MODELING OF RAPIDLY ROTATING THERMAL CONVECTION USING VORTICITY AND VECTOR POTENTIAL

ZDENĚK MISTR[1], CTIRAD MATYSKA[1*], DAVID A. YUEN[2]

ABSTRACT

We have used a numerical scheme based on higher-order finite differences to investigate effects of adiabatic heating and viscous dissipation on 3-D rapidly rotating thermal convection in a Cartesian box with an aspect-ratio of 2×2×1. Although we omitted coupling with the magnetic field, which can play a key role in the dynamics of the Earth's core, the understanding of non-linear rotating convection including realistic thermodynamic effects is a necessary prerequisite for understanding the full complexity of the Earth's core dynamics. The system of coupled partial differential equations has been solved in terms of the principal variables vorticity $\boldsymbol{\omega}$*, vector potential* $\mathbf{A}$ *and temperature T. The use of the vector potential* $\mathbf{A}$ *allows the velocity field to be calculated with one spatial differentiation in contrast to the spheroidal and toroidal function approach. The temporal evolution is governed by a coupled time-dependent system consisting of* $\boldsymbol{\omega}$ *and T. The equations are discretized in all directions by using an eighth-order, variable spaced scheme. Rayleigh number Ra of* 10^6*, Taylor number Ta of* 10^8 *and a Prandtl number Pr of 1 have been employed. The dissipation number of the outer core was taken to be 0.2. A stretched grid has been employed in the vertical direction for resolving the thin shear boundary layers at the top and bottom. This vertical resolution corresponds to around 240 regularly spaced points with an eighth-order accuracy. For the regime appropriate to the Earth's outer core, the dimensionless surface temperature* T_0 *takes a large value, around 4. This large value in the adiabatic heating/cooling term is found to cause stabilization of both the temperature and velocity fields.*

Keywords: High Rayleigh number, 3-D convection, higher-order finite differences, rotating fluid, finite Prandtl number.

1. INTRODUCTION

The geodynamo problem is now recognized to be a very challenging computational problem in geophysical fluid dynamics (e.g., *Roberts, 1992; Braginsky and Roberts, 1995; Glatzmaier and Roberts, 1995,1996; Kuang and Bloxham, 1997*) because of its

[1] Department of Geophysics, Faculty of Mathematics and Physics, Charles University, V Holešovičkách 2, 180 00 Praha 8, Czech Republic

[*] Corresponding author (Ctirad.Matyska@mff.cuni.cz)

[2] Department of Geology and Geophysics and Minnesota Supercomputing Institute, University of Minnesota, Minneapolis, MN 55415-1227, USA

multiple-scale nature. The flow involves high Rayleigh number thermal-chemical convection in a rapidly rotating, magnetohydrodynamic system. There has been a surge of interest in the dynamo problem from various points of view (e.g., *Christensen et al., 1998; Busse et al., 1998*). Most of the work on numerical simulations have been based on spherical geometry (*Glatzmaier and Roberts, 1995,1996; Kuang and Bloxham, 1997*). *St. Pierre (1996)* and *Velímský and Matyska (2000)* have studied the finite-amplitude geodynamo problem using Cartesian geometry.

In this work we will focus on a simpler system involving thermal convection in a rotating system but will consider the effects of adiabatic heating on the 3-D flow structure. We will present three-dimensional numerical simulations of thermal convection in a chemically homogeneous, rapidly rotating system. We will concentrate on the effects of rotation, dissipation and adiabatic heating on the pattern of the flow. A major trade-off exists between these two approaches in modeling the rotating spherical-shell convection. Global models simulate fluid motions in the whole spherical-shell domain (see, e.g., *Glatzmaier and Roberts, 1995*). On the other hand, local models (see, e.g., *Brummell et al., 1995,1998*) have been used extensively in astrophysics. They restrict the computational domain to a small (but still three-dimensional) subsection of the global domain. This allows for more detailed modeling and/or choosing more realistic parameters at the same computational cost. The disadvantage of these local models is that the new boundaries demarcating the domain produce artificial effects, which can significantly influence the results of the modeling.

In this paper we will present a local model simulating the fluid motion in the 3-D Cartesian box based on the higher-order finite-difference schemes newly developed by *Fornberg (1996)*. We have employed a higher-order finite-difference method with unevenly spaced grid points. With the exception of *Velímský and Matyska (2000)*, most of the existing dynamo codes are based on spectral-transform methods (*Glatzmaier and Roberts, 1995,1996*) or finite-difference-spectral-transform techniques (*Kuang and Bloxham, 1997,1999*). Moreover, all of these authors have employed the toroidal and spheroidal potential approach, which means that the velocity fields must be obtained by subsequent spatial differentiation. In this local domain we approximate the radial gravitational field by a homogeneous one. By choosing suitable local directions of the gravitational acceleration and rotational vector, this model can represent various parts of the outer core (see Fig. 1).

The paper is divided into four parts. In Section 2, we briefly describe the model we have used to simulate the fluid motion in the context of the outer core dynamics. We will start with the general laws of fluid mechanics. Assuming several approximations, we will express the basic equations in a special form. Finally, we will introduce dimensionless variables, modify the equations to vorticity-vector potential formulation which is suitable for computation and describe the higher-order finite-difference method used in solving these equations. Some results of the numerical modeling are presented in Section 3. We will describe the numerical and physical parameters of all cases. We will start with the basic equations and then concentrate on the effects of rotation, dissipation and adiabatic heating. The concluding remarks concerning this method and the results obtained are given in Section 4.

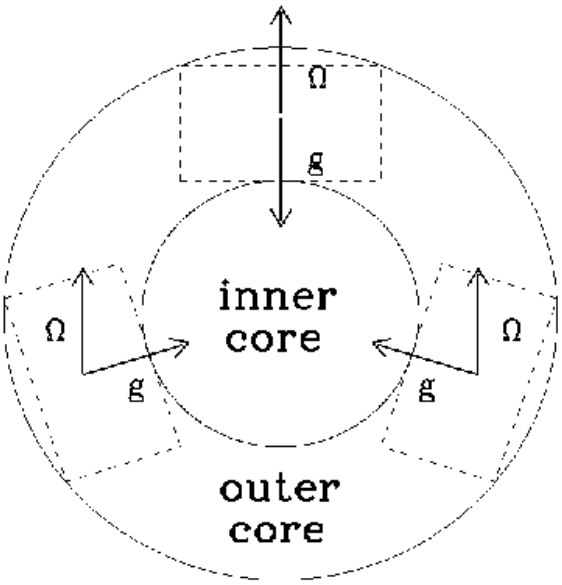

Fig. 1. Possible positions of local-area computational domains (meridional cross-section). **Ω** and ***g*** denote the vectors of rotation and gravitational acceleration, respectively.

2. GOVERNING EQUATIONS

2.1. General Equations

The axioms controling the motion of the continuum are the conservation of mass, momentum, moment of momentum and energy. The partial differential equations are (all symbols used can be found in Tab. 1)

$$\frac{\partial \rho}{\partial t} + \nabla \cdot (\rho \boldsymbol{u}) = 0\,, \tag{1}$$

$$\nabla \cdot \tau + \boldsymbol{f} = \boldsymbol{S}\,, \tag{2}$$

$$\tau_{ij} = \tau_{ji}\,, \tag{3}$$

$$\rho T\left(\frac{\partial s}{\partial t} + \boldsymbol{u} \cdot \nabla s\right) = \nabla \cdot (k \nabla T) + \sigma : \nabla \boldsymbol{u} + Q\,. \tag{4}$$

Table 1. List of the symbols used.

Symbol	Meaning	Unit SI
t	time	s
$\boldsymbol{u}$	velocity	ms^{-1}
T	temperature	K
P	pressure	Pa
Π	difference between the pressure and the hydrostatic pressure	Pa
ρ	density	kgm^{-3}
s	density of entrophy	$m^2s^{-2}K^{-1}$
τ	stress tensor	Pa
σ	deviatoric stress	Pa
η	dynamic viscosity	Pa s
ν	kinematic viscosity	m^2s^{-1}
$\boldsymbol{g}$	gravitational acceleration	ms^{-2}
$\boldsymbol{\Omega}$	vector of rotation	s^{-1}
C_P	specific heat at constant pressure	$m^2s^{-2}K^{-1}$
k	thermal conductivity	kg m $s^{-3}K^{-1}$
κ	thermal diffusivity	m^2s^{-1}
α	thermal expansivity	K^{-1}
Q	internal heating rate	kg $s^{-3}m^{-1}$
d	depth of the box	m
a_x, a_y	aspect ratios in x and y directions	
$\boldsymbol{A}$	vector potential	
$\boldsymbol{\omega}$	vorticity	
$\boldsymbol{e}_x$, $\boldsymbol{e}_y$, $\boldsymbol{e}_z$	Cartesian base vectors	
Ra	Rayleigh number	
Ta	Taylor number	
Pr	Prandtl number	
Dn	dissipation number	
T_1, T_0	temperature at the bottom and the top of the box	K
T_Δ	surface temperature over temperature drop	
$\boldsymbol{k}$	unit vector of rotation	
β	angle between $\boldsymbol{e}_z$ and $\boldsymbol{k}$	rad

Here velocity $\boldsymbol{u}$, temperature T, density ρ and the density of entropy s are the variables required to describe the motion of the chemically homogeneous fluid. The volume and inertial forces are denoted by $\boldsymbol{f}$ and $\boldsymbol{S}$, respectively, k is the thermal conductivity, which is strongly temperature dependent because of the liquid iron, and Q denotes the internal heat sources. Stress tensor τ and deviatoric stress σ are determined by the rheology of the fluid.

2.2. Model Specification

The aim of this work is to simulate the flow of a slightly viscous fluid with inertia in a 3-D rotating Cartesian box. The computational domain is situated in the homogeneous

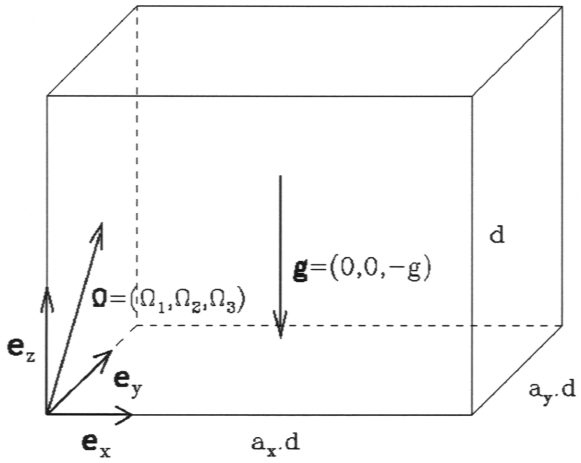

Fig. 2. Cartesian computational domain.

gravitational field and heated from below (see Fig. 2). By choosing suitable parameters of the model (see below), we will find the consequences of the modeling for the fluid motion in the outer core. From this point of view, the 3-D box here represents a local volume of the outer core. The top and the bottom of the box mimic a part of the core-mantle boundary and inner-core boundary, respectively. These assumptions specify some of the terms in the general equations (1)–(4).

The only volume force in momentum equation (2) is the gravitational force, i.e.

$$\boldsymbol{f} = \rho \boldsymbol{g} = -\rho g \boldsymbol{e_z} . \tag{5}$$

The effect of rotation is included by treating the Coriolis force as part of the inertial forces

$$\boldsymbol{S} = \rho \left(\frac{\partial \boldsymbol{u}}{\partial t} + \boldsymbol{u} \cdot \nabla \boldsymbol{u} + 2\boldsymbol{\Omega} \times \boldsymbol{u} \right). \tag{6}$$

We assume that rotation vector $\boldsymbol{\Omega}$ is a constant. The centrifugal acceleration can be neglected for the range of parameters used in the model.

For the equation of state, the extended Boussinesq approximation is employed (*Christensen and Yuen, 1985; Christensen 1989*), which comes from the inelastic approximation (*Jarvis and McKenzie, 1980*). The principal assumption of this approximation is that density is not explicitly dependent on pressure and depends only weakly on temperature, i.e. density can be expressed as a linear function of temperature, namely

$$\rho = \rho_0 \left(1 - \alpha (T - T_0)\right), \tag{7}$$

where ρ_0 is a reference density, α is the thermal expansivity and T_0 is a reference temperature. In the Earth, the non-hydrostatic pressure is small compared to the hydrostatic pressure. Thus the dependence of the density on the pressure can be implicitly considered as the dependence of ρ_0 on z. The variation of density with temperature can be neglected in both the conservation of mass and the energy equations of the mantle and outer core (*Jarvis and Peltier, 1989*). On the other hand, this variation has an important role in the term of the gravitational force in equation (2).

The specific entropy of the fluid depends not only on the temperature but also on the hydrostatic pressure in the extended Boussinesq approximation. Thermodynamic properties can be expressed by means of the two dimensionless parameters: Grüneisen ratio $\gamma = \alpha K_T / (\rho_0 C_p)$, with K_T being the isothermal bulk modulus, and the dissipation number $Dn = \alpha g d / C_p$, where d is the scaling parameter of length (usually the thickness of the layer). Here we have taken the limit γ tending large but Dn remaining finite (*Christensen and Yuen, 1985*). It is like physically taking the bulk modulus to be infinite. Since K_T does not influence the form of the heat equation (4), and since bulk modulus K_T and dissipation number Dn are thermodynamically independent parameters (*Tritton, 1988*), the continuity equation (1) can be expressed in the incompressible form, where the dependence of ρ_0 on depth is omitted, while the adiabatic heating/cooling as well as dissipation are considered in the energy equation (4).

If we consider all these assumptions, we can modify the general equations (1)–(4). First, the conservation of mass has the following incompressible form:

$$\nabla \cdot \boldsymbol{u} = 0 , \tag{8}$$

which means that the velocity can be expressed as a solenoidal field. Second, in equations (5) and (6) we specify the volume and inertial forces, respectively. Assuming the extended Boussinesq approximation and Newtonian rheology, the conservation of momentum (momentum equation) takes the form

$$\rho_0 \frac{\partial \boldsymbol{u}}{\partial t} = -\rho_0 \boldsymbol{u} \cdot \nabla \boldsymbol{u} - 2\rho_0 \boldsymbol{\Omega} \times \boldsymbol{u} - \nabla \Pi + \eta \nabla^2 \boldsymbol{u} + \rho_0 \alpha g (T - T_0) \boldsymbol{e_z} , \tag{9}$$

where Π is the difference between the prevailing pressure and the hydrostatic pressure, i.e. $\Pi = P - h\rho_0 g$, h is the depth. Finally, the conservation of energy can be expressed in terms of thermodynamic variables ρ, T and P. Under the assumptions mentioned above, its form is (see also the discussion in *Christensen, 1989*)

$$\rho_0 C_P \frac{\partial T}{\partial t} = k \nabla^2 T - \rho_0 C_P \boldsymbol{u} \cdot \nabla T + \sigma : \nabla \boldsymbol{u} - \rho_0 g \alpha T u_z + Q , \tag{10}$$

where thermal conductivity k is taken to be a constant. In this approximation, only the influence of the hydrostatic pressure is taken into account by means of adiabatic heating $-\rho_0 g \alpha T u_z$. In this work we will assume $Q = 0$, i.e. we will neglect the effects of internal heating, which may not be true in the outer core (*Breuer and Spohn, 1993*).

We have thus obtained the equations describing the motion of the fluid inside the box. To be able to solve them we need to prescribe boundary and initial conditions for all variables, i.e. three components of velocity, temperature and pressure.

In our model, we choose constant temperatures at both the bottom and the top of the box. We assume zero heat flux through the sidewalls. From these assumptions, it follows that

$$T(top) = T_0\,, \qquad T(bottom) = T_1\,,$$

$$\boldsymbol{n} \cdot \nabla T(sidewalls) = 0\,. \tag{11}$$

Here $\boldsymbol{n}$ denotes the unit vector perpendicular to the surface.

For the velocity and pressure the impermeable, free-slip boundary condition is applied to all sides, i.e.

$$\boldsymbol{n} \cdot \boldsymbol{u} = 0\,, \tag{12}$$

$$\tau \cdot \boldsymbol{n} - \big((\tau \cdot \boldsymbol{n}) \cdot \boldsymbol{n}\big)\boldsymbol{n} = 0\,. \tag{13}$$

Equation (12) expresses zero mass flux through the sides. Fluid cannot escape from the box. Equation (13) requires the tangential stresses to vanish at the sides of the box.

2.3. Dimensionless Variables

In the previous section we derived equations (8)–(10) which, together with boundary conditions (11)–(13), determine the fluid dynamical behavior. In these equations there are many parameters and their combinations. This makes the situation somewhat ambiguous. The aim of this section is to describe minimum set of combinations of parameters needed to fully describe the behavior of the fluid for the extended Boussinesq approximation introduced here.

The standard way is to introduce the dimensionless variables. When choosing suitable values of scaling factors for each variable one can reduce the number of parameters to a minimum set of their combinations. The set of scaling factors used in this paper involving the finite Prandtl number and rotation is shown in Tab. 2 (for a different scaling used in mantle convection with the infinite Prandtl number and no rotation see, e.g., *Jarvis and Peltier, 1989; Malevsky, 1996*). From these new dimensionless variables (using the same symbols) we obtain the following form of equations (8)–(10)

$$\nabla \cdot \boldsymbol{u} = 0\,, \tag{14}$$

$$\frac{\partial \boldsymbol{u}}{\partial t} = -\boldsymbol{u} \cdot \nabla \boldsymbol{u} - (Ta)^{\frac{1}{2}}\, \boldsymbol{k} \times \boldsymbol{u} - \nabla \Pi + \nabla^2 \boldsymbol{u} + Ra(Pr)^{-1} T \boldsymbol{e_z}\,, \tag{15}$$

$$\frac{\partial T}{\partial t} = (Pr)^{-1} \nabla^2 T - \boldsymbol{u} \cdot \nabla T + PrDn(Ra)^{-1} (\sigma : \nabla \boldsymbol{u}) - Dn(T + T_\Delta)\, u_z\,. \tag{16}$$

Rayleigh number *Ra*, Taylor number *Ta*, Prandtl number *Pr*, dissipation number *Dn*, the dimensionless surface temperature over temperature drop T_Δ and the unit vector of rotation $\boldsymbol{k}$ form the new set of parameters. Their definitions are:

Table 2. Scaling factors used to derive dimensionless equations. The new, dimensionless variables are denoted with asterisk. Symbols used here are explained in Table 1.

Symbol	Meaning	Scaling factor	Relationship
t	time	d^2/ν	$t = t^* d^2/\nu$
x	length	d	$x = dx^*$
$\boldsymbol{u}$	velocity	ν/d	$\boldsymbol{u} = \boldsymbol{u}^* \nu/d$
P	pressure	$\eta\nu/d^3$	$P = P^* \eta\nu/d^3$
T	temperature	$T_1 - T_0$	$T = T_0 + (T_1 - T_0)T^*$

$$Ra = \frac{\alpha g d^3 (T_1 - T_0)}{\kappa\nu}, \qquad Ta = \frac{4d^4\Omega^2}{\nu^2}, \qquad Pr = \frac{\nu}{\kappa},$$

$$Dn = \frac{\alpha g d}{C_P}, \qquad T_\Delta = \frac{T_0}{(T_1 - T_0)},$$

where $\nu = \eta/\rho_0$ is the kinematic viscosity, $\kappa = k/(\rho_0 C_P)$ is the thermal diffusivity and d is the depth of the box.

We will use only the following positions of vector $\boldsymbol{k}$:

$$\boldsymbol{k} = (\sin\beta, 0, \cos\beta), \qquad \beta \in \left\langle 0, \frac{\pi}{2} \right\rangle, \tag{17}$$

where β is the angle between base vector $\boldsymbol{e}_z$ and the vector of rotation $\boldsymbol{\Omega}$. As described above, the box represents a local area of the outer core. This range of positions of vector $\boldsymbol{k}$ describes the situations in all parts of the outer core.

2.4. The Formulation Based on Vorticity and Vector Potential

In this section, we will reduce the system of five equations (14)–(16) for five dimensionless variables $\boldsymbol{u}$ (three components), T and Π to a system of four equations by introducing vorticity and vector potential.

From the equation of continuity (14) it follows that the velocity is a solenoidal field. Thus the velocity, which has both toroidal and poloidal components, can be determined by vector function $\boldsymbol{A}$ which is defined as

$$\boldsymbol{u} = \nabla \times \boldsymbol{A}\,. \tag{18}$$

We emphasize that the velocity field $\boldsymbol{u}$ calculated from eqn. (18) is represented more accurately than it would be using the spheroidal and toroidal potential approach, since the potentials include higher-order spatial derivatives, because of the use of higher-order differential operators. This approach of using a vector potential and vorticity in 3-D

systems has been shown by (*Malevsky, 1996; Malevsky and Thomas, 1997*) to be very efficient for parallel computing in thermal convection and meteorological problems. Let us assume the additional condition on vector function $\boldsymbol{A}$ takes the form

$$\nabla \cdot \boldsymbol{A} = 0 . \tag{19}$$

The vorticity can be defined as

$$\boldsymbol{\omega} = \nabla \times \boldsymbol{u} . \tag{20}$$

From equations (18)–(20) we get the relationship between the vector potential and the vorticity vector.

$$\boldsymbol{\omega} = -\nabla^2 \boldsymbol{A} . \tag{21}$$

Thus the vector potential can be obtained from the vorticity by solving the three Poisson equations (21).

Now let us apply operator $\nabla\times$ to momentum equation (15). We obtain

$$\begin{aligned} \frac{\partial \omega}{\partial t} = {} & \boldsymbol{\omega} \cdot \nabla \boldsymbol{u} - \boldsymbol{u} \cdot \nabla \boldsymbol{\omega} + \nabla^2 \boldsymbol{\omega} + (Ta)^{\frac{1}{2}} \sin\beta \frac{\partial \boldsymbol{u}}{\partial x} + (Ta)^{\frac{1}{2}} \cos\beta \frac{\partial \boldsymbol{u}}{\partial z} \\ & + Ra(Pr)^{-1} (\nabla \times Te_z) \end{aligned} \tag{22}$$

This form of the momentum equation with velocity vector $\boldsymbol{u}$ to be calculated from eqn. (18) contains no term with the modified pressure Π. Assuming that $\boldsymbol{u} = \boldsymbol{u}(\boldsymbol{A})$, $\boldsymbol{\omega} = \boldsymbol{\omega}(\boldsymbol{A})$, energy equation (16) and the reformulated momentum equation (22) constitute a system of four equations in the four variables $\boldsymbol{A}$ and T. In fact, variables $\boldsymbol{\omega}$ and T will be integrated simultaneously in time (see below). Vector $\boldsymbol{A}$ will be computed by solving the Poisson equations (21).

In Section 2.2, we prescribed the boundary conditions for the dimensional variables $\boldsymbol{u}$, P and T that need to be reformulated for the new dimensionless variables; now eqn. (11) yields:

$$\begin{aligned} & T(z=0) = 1 , \qquad T(z=1) = 0 , \\ & \frac{\partial T}{\partial x}(x = 0, a_x) = 0 , \quad \frac{\partial T}{\partial y}(y = 0, a_y) = 0 . \end{aligned} \tag{23}$$

The boundary conditions for the vector potential can be used in the form (*Malevsky, 1996*)

$$\omega_n = \omega_q = \omega_t = \frac{\partial A_n}{\partial n} = A_q = A_t = 0 . \tag{24}$$

Here n, t and q denote, in the following order, the normal and the two tangential components.

2.5. Numerical Algorithm

We solve the system of evolutionary equations (16) and (22) as follows:

1. Applying the initial conditions in the form

$$T(x, y, z, t = 0) = f_1(x, y, z),$$

$$\boldsymbol{u}(x, y, z, t = 0) = \boldsymbol{f}_2(x, y, z),$$

$$\boldsymbol{\omega}(x, y, z, t = 0) = \nabla \times \boldsymbol{f}_2(x, y, z).$$

2. Computing the time step.
3. Computing T and $\boldsymbol{\omega}$ for the new time level using the system of equations (16) and (22).
4. Computing vector potential $\boldsymbol{A}$ for the new time level using the Poisson equations (21).
5. Computing velocity $\boldsymbol{u}$ for the new time level using the definition of vector potential (18)
6. Reverting to 2.

In this study we covered the box with a generally irregular spatial grid, where more points are located at the horizontal boundary layers. The grid point values are used instead of continuous fields to solve the system of equations (16) and (22).

To approximate spatial derivatives we employed a finite difference scheme. Let us consider a one-dimensional function $f(x)$ discretized at points x_i, $i = 0, N$. To obtain the n^{th} order finite difference scheme (n is even) to approximate the k^{th} derivative at point x_j we interpolate function $f(x)$ by a polynomial of the n^{th} order denoted P_j^n. Now we can approximate the k^{th} derivative of $f(x)$ at point x_j by the corresponding derivate of polynomial $P_j^n(x)$. Hence,

$$\frac{d^k f}{dx^k}(x_j) \doteq \sum_{i=j-\frac{n}{2}}^{j+\frac{n}{2}} W_{ji}^{nk} f(x_i), \tag{25}$$

where weights W_{ji}^{nk} can be calculated easily. We note that using the n^{th} order finite difference scheme, we need $n + 1$ values of f to calculate the approximation of the k^{th} derivative of f.

One can generalize this method to three-dimensional fields. The application of this method to mantle convection can be found in *Moser (1994)* and *Larsen et al. (1997)*. Applications to the sphere have been made by *Merilees (1973,1974)*, *Fornberg (1995)* and *Fornberg and Merrill (1997)*. We only need to compute the weights for each direction separately. The efficient algorithm for calculating weights W_{ji}^{nk} was developed by *Fornberg (1992)*. We have used his Fortran subroutine (*Fornberg, 1996*) for fast generation of the weights. We have employed an 8^{th} order finite-difference scheme for this problem because *Larsen et al. (1997)* found by a detailed comparison that 8^{th} order

schemes provide much greater accuracy in the higher Rayleigh number regime than lower-order finite-difference methods.

The approximation of derivatives for grid points near the boundaries of the box represents a special problem. We have expanded the grid outside the box. Because of the 8^{th} order finite difference scheme, we have defined four levels of grid points symmetrically beyond each boundary. We then defined the values of each 3-D field at the new grid points. The new values were chosen to satisfy the corresponding boundary condition, i.e. symmetrically for the zero flux condition (the Neumann condition) and antisymmetrically for the condition involving zero values (the Dirichlet condition). We note that the one-sided Fornberg scheme retains the same order of accuracy at the boundaries and is an unique advantage over other variable spacing finite-difference schemes.

Now we will describe the numerical method we have used to solve the Poisson equations (21). Let us consider an elliptic partial differential equation,

$$\left(D_x + D_y + D_z\right) u = -f \ , \tag{26}$$

where D_x, D_y and D_z are the x, y and z components of the elliptic differential operator, f is a given 3-D field and u is 3-D field which should be solved. In using the finite difference scheme to solve equation (26), one can reorganize the discretized fields u and f into one-dimensional vectors and approximate the differential operations by matrix-vector multiplications:

$$\left(\boldsymbol{D}_x + \boldsymbol{D}_y + \boldsymbol{D}_z\right) u = -f \ . \tag{27}$$

Here matrices $\boldsymbol{D}_\alpha$ represent approximations of operators D_α.

The Alternating Direction Implicit (ADI) scheme (*Douglas and Rachford, 1956*) is an iterative method for solving equation (27). In a 3-D situation each iteration has three steps which can be expressed as:

$$(\boldsymbol{I} - \delta \boldsymbol{D}_x)\, u^{(l+1/3)} = \left(\boldsymbol{I} + \delta\left(\boldsymbol{D}_y + \boldsymbol{D}_z\right)\right) u^{(l)} + \delta f \ , \tag{28}$$

$$\left(\boldsymbol{I} - \delta \boldsymbol{D}_y\right) u^{(l+2/3)} = u^{(l+1/3)} - \delta \boldsymbol{D}_y u^{(l)} \ , \tag{29}$$

$$(\boldsymbol{I} - \delta \boldsymbol{D}_z)\, u^{(l+1)} = u^{(l+2/3)} - \delta \boldsymbol{D}_z u^{(l)} , \tag{30}$$

where $\boldsymbol{I}$ is the identity matrix, index l describes the number of iterations and δ is a convergence parameter.

We have used the ADI method for the three Poisson equations (21). They can be modified to read:

$$\left(\frac{\partial^2}{\partial x^2} + \frac{\partial^2}{\partial y^2} + \frac{\partial^2}{\partial z^2}\right) A_\alpha = -\omega_\alpha \ , \qquad \alpha \in \{x, y, z\}. \tag{31}$$

Hence, matrices $\boldsymbol{D}_\alpha$ represent the finite difference approximations of the corresponding 2nd derivatives. These matrices are banded and their non-zero parts are filled out with the weights (see eqn. 25). This property makes the ADI algorithm more efficient and also much easier to parallelize.

For the grid configurations and Rayleigh and Taylor numbers used in this paper we found experimentally that for $\delta = 0.02$ the convergence of the ADI iterative scheme is the best. Usually 1 to 10 iterations were necessary to reduce the relative error (according to the L_2 norm) to 5×10^{-7}.

We have employed the 2nd order Runge-Kutta method to evolve equations (16) and (22) in time. Let us denote the right-hand sides of these equations g_1 and $\boldsymbol{g}_2$, respectively, i.e.

$$\frac{\partial T}{\partial t} = g_1(T, \boldsymbol{\omega}), \tag{32}$$

$$\frac{\partial \boldsymbol{\omega}}{\partial t} = \boldsymbol{g}_2(T, \boldsymbol{\omega}). \tag{33}$$

Using the Poisson equations (21) together with the prescribed boundary conditions we see that vector potential $\boldsymbol{A}$ is a function of the vorticity, i.e. $\boldsymbol{A} = \boldsymbol{A}(\boldsymbol{\omega})$. This allows us to express explicitly the dependence of right-hand sides g_1 and $\boldsymbol{g}_2$ on the vorticity instead of the vector potential or velocity.

We have employed a special form of the 2nd order Runge-Kutta method, called the modified Euler method (*Vitásek, 1987*). For simplicity, we will show its application to the energy equation. Let index *n* denote the discretized time levels. This semi-explicit scheme then takes the form:

$$T_{n+1} = T_n + \frac{1}{2} dt\left[g_1(T_n, \boldsymbol{\omega}_n) + g_1(T'_{n+1}, \boldsymbol{\omega}'_{n+1})\right], \tag{34}$$

where

$$T'_{n+1} = T_n + g_1(T_n, \boldsymbol{\omega}_n)dt\,, \quad \boldsymbol{\omega}'_{n+1} = \boldsymbol{\omega}_n + \boldsymbol{g}_2(T_n, \boldsymbol{\omega}_n)dt\,,$$

and *dt* is the time step.

The right-hand sides g_1 and $\boldsymbol{g}_2$ were approximated by the higher-order finite difference scheme. Time step *dt* was determined by the Courant-Levy-Friedrichs criterion in the form:

$$dt = C \min\left[\frac{\min(\Delta x)}{\max(u_x)}, \frac{\min(\Delta y)}{\max(u_y)}, \frac{\min(\Delta z)}{\max(u_z)}\right], \tag{35}$$

where Δx, Δy and Δz denote grid distances in the corresponding directions and *C* denotes a numerical constant, which is determined experimentally. We have used values ranging from 0.2 to 0.4.

Table 3. Values of relatively well-known parameters at the core-mantle boundary (CMB) and inner-core boundary (ICB). After *Braginsky and Roberts (1995).*

Symbol	Parameter	SI unit	CMB	ICB
r	radius	m	3.48×10^6	1.22×10^6
Ω	angular velocity	rad s^{-1}	7.3×10^{-5}	7.3×10^{-5}
g	gravitational acceleration	m s^{-2}	10.68	4.40
T	temperature	K	4000	5300
α	thermal expansivity	K^{-1}	1.8×10^{-5}	1.0×10^{-5}
C_P	specific heat	J $K^{-1}kg^{-1}$	848	826

3. NUMERICAL RESULTS

The parametric values of some relatively well-known outer core properties are listed in Table 3. Unfortunately, our knowledge of kinematic viscosity ν and thermal diffusivity κ is poor. If we take rough estimates $\nu \approx 10^{-6}$, $\kappa \approx 10^{-6}$ (*Cardin and Olson, 1994; Braginsky and Roberts, 1995*), we obtain the following estimates of orders of the dimensionless numbers: $Ra \approx 10^{30}$, $Ta \approx 10^{29}$, $Pr \approx 1$, $Dn \approx 0.1$ and $T_\Delta \approx 1$. The values of Ra and Ta are completely beyond present-day computational reach. Attainable values are several orders of magnitude less (note that the effective "weight" of the Coriolis term is $(Ta)^{1/2}$). We conducted our simulations with $Ra = 10^6$ and $Ta = 10^8$. We have chosen other dimensionless parameters satisfying the estimates mentioned above, namely $Pr = 1$, $Dn = 0.2$ and $T_\Delta = 4$. We emphasize that for the outer core T_Δ is much greater than 1, since the surface temperature at CMB is much greater than the temperature increase across the outer core (*Boehler, 1996*). The angle between vectors $\boldsymbol{e}_z$ and $\boldsymbol{\Omega}$ was taken from the set $\beta \in \{0°,45°,90°\}$.

Table 4. List of parameters for various configurations.

Number	Notation	Ra	Pr	Ta	β	Dn	T_Δ
1	Bas	10^6	1	0	---	0	---
2	Dis	10^6	1	0	---	0.2	4
3	Rot0	10^6	1	10^8	0°	0	---
4	Rot45	10^6	1	10^8	45°	0	---
5	Rot90	10^6	1	10^8	90°	0	---
6	Dis0	10^6	1	10^8	0°	0.2	4
7	Dis45	10^6	1	10^8	45°	0.2	4
8	Dis90	10^6	1	10^8	90°	0.2	4

Table 4 contains a list of all the cases studied. All of them were calculated in a box 2×2×1, i.e. $a_x = 2$, $a_y = 2$. To resolve the thin boundary layers, we have employed an irregular grid spacing along the vertical direction. The grid distances decrease 4 times from the middle to the top (bottom) surface of the box. Thus effectively the horizontal boundary layers have a resolution characteristic of 240 regularly spaced points with extremely high-order accuracy along the vertical direction. The grid spacing in horizontal directions was regular. We used a 71×71×71 grid configuration for all cases. In fact, the number of grid points was 79×79×79 using a central finite difference scheme for points near the boundaries.

3.1. Basic Cases

In this section we will present the results of the first two cases denoted as *Bas* and *Dis* (see Tab. 4).

In Fig. 3 we present a typical "snapshot" of case *Bas* with well-developed time-dependent temperature and velocity fields at $t = 0.043$. Thin boundary layers are developed at the top and the bottom of the box. In these layers instabilities result in vertical motions driven by the buoyancy forces. Inertial forces cause the horizontal motions, vertical motions with strong rotation and sometimes also the disconnection of these hot upwellings (plumes) and cold downwellings. This mechanism of heat transfer by convection is much more efficient than conduction. Conduction plays an important role at the top and bottom surfaces, where the thin boundary layers with high vertical temperature gradients promote the vertical heat transfer.

Changing the values of *Dn* and T_Δ to 0.2 and 4.0, respectively, in the *Dis* case radically stabilized both the temperature and the velocity fields, and the system evolved toward a stationary solution. Moreover, the temperature field was very close to a static one, characterized by a conductive temperature profile $T(x,y,z,t) = 1 - z$. What is the reason for this behavior? In the *Bas* case the part of the convective term $-u_z(\partial T/\partial z)$ of energy equation (16) describes the local temperature change due to vertical motions of the fluid - the main mechanism of heat transfer between the bottom and the top of the box. In the *Dis* case the adiabatic term $-Dn(T + T_\Delta)u_z$ causes thermodynamic cooling of these hot upwellings (heating of the cold downwellings) due to the decrease (increase) of the

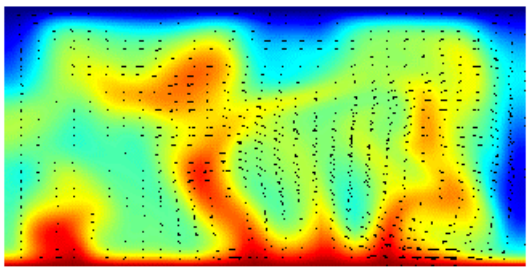

Fig. 3. Temperature field (background) and velocity components (vectors in foreground) in a plane perpendicular to the *x*-axis in a middle of the box (Bas case, time = 0.0234).

hydrostatic pressure. Let us assume a conductive profile of the temperature in both the convective term and the adiabatic term. We then obtain the values of u_z and $-G(z)u_z$, respectively, where $G(z) = Dn(1 - z + T_\Delta)$. Using the prescribed values of $Dn = 0.2$ and $T_\Delta = 4.0$, we get $G = 0.8$ at the top and $G = 1.0$ at the bottom of the box, i.e. the adiabatic gradient is identical with the conduction gradient at the bottom of the box, and both gradients are still close at the top. In other words, this estimate states that the adiabatic cooling/heating nearly compensates the vertical advection of heat. The adiabatic cooling/heating can thus be the fundamental physical mechanism in thermal convection under the core conditions. In the Rayleigh-Benard convection without this physical mechanism the stability of convection is controlled by the rotational speed (*Demircan et al., 2000*).

3.2. Effects of Rotation

In this section we will describe the results of the cases concerning rapidly rotating convection (see cases Rot0, Rot45 and Rot90 in Tab. 4).

Let us first take into account the following situations:

(i) The fluid motion is geostrophic, i.e. the Coriolis force is fully balanced by the gradient of the pressure, and thus the momentum equation takes the following form:

$$-\nabla P = \rho\left(2\boldsymbol{\Omega}\times\boldsymbol{u}\right), \tag{36}$$

(ii) baroclinic vector $\boldsymbol{b}$ is identically zero, i.e.

$$\boldsymbol{b} = \frac{\left(\nabla\rho\times\nabla P\right)}{\rho^2} = 0\,. \tag{37}$$

If these two conditions are satisfied, the velocity in planes perpendicular to $\boldsymbol{\Omega}$ are independent of the coordinate parallel to $\boldsymbol{\Omega}$. This constraint is known as the Taylor-Proudman theorem (*Pedlosky, 1987*).

The question arises whether conditions (36), (37) are satisfied in some of the studied cases. Since we assume that the density is constant (with the exception of the term of the gravity force in the momentum equation), condition (ii) is satisfied. To explore the validity of condition (i) we will discuss the relative weights of the terms in the momentum equation. The estimates of ratios of the viscous term ($\eta\nabla^2\boldsymbol{u}$) and the inertial term ($\rho_0 \frac{D\boldsymbol{u}}{Dt}$) to the Coriolis force are given by the Ekman number E and Rossby number ε, respectively (*Pedlosky, 1987*). Their definitions are:

$$E = \frac{\nu}{2\Omega L^2}\,, \qquad \varepsilon = \frac{U}{2\Omega L}\,, \tag{38}$$

where L is a characteristic length scale and U is the characteristic velocity of the motion. If we characterize the length scale by the depth of the box d and the velocity scale by the values from the *Bas* case ($\approx 10^2 \frac{\nu}{d}$), we obtain $E \approx 10^{-4}$ and $\varepsilon \approx 10^{-2}$. With the same procedure, we can estimate the ratio of the buoyancy force to the Coriolis force as a number N:

$$N = \frac{\alpha g (T_1 - T_0)}{2\Omega U} \approx 1 . \tag{39}$$

Therefore, the buoyancy force is strong enough to produce the fluid motion parallel to **Ω** if the gravity acceleration and the vector of rotation are not perpendicular.

In the Rot90 case the gravity field has a zero contribution parallel to **Ω**. Fig. 4 shows that the obtained pattern of both the temperature and velocity fields is really independent of this direction. The convective circulation of the fluid in the planes perpendicular to **Ω** "interacts" with the Coriolis force.

In contrast to the Rot90 case, if the gravity field is parallel to the rotational axis (case Rot0), the buoyancy forces act exactly opposite to the two-dimensional tendency of the Taylor-Proudman theorem. In other words, this configuration of gravity field and rotational axis makes the thermal convection more difficult. This fact was demonstrated by global models of rotating spherical-shell convection without adiabatic heating/cooling (e.g., *Sun and Schubert, 1995*). In these models the polar areas were relatively calm and thermal convection occurred mainly in other parts of the spherical shell. In this local model we obtained a similar effect. The temperature and velocity fields in horizontal plane in the middle of the box are shown in Fig. 5.

Because of the impermeable boundary condition, the Coriolis force is constrained to the sidewalls. Vertical convective motion occurs only on these sidewalls, while the central area of the box is characterized by constant temperature and low velocities. The Coriolis forces tend to produce relative circulation in a sense opposite to the prescribed rotation

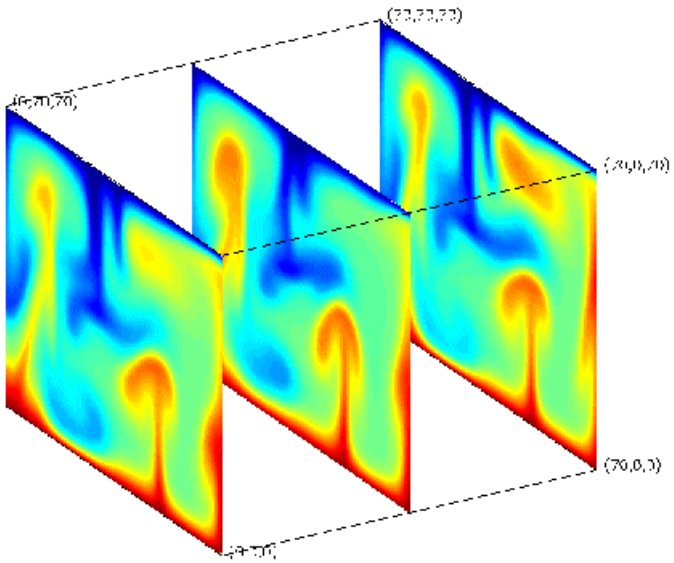

Fig. 4. Temperature fields in (*z*,y*)* planes, $x = 0$, $x = a_x/2$ and $x = a_x$ (Rot90 case).

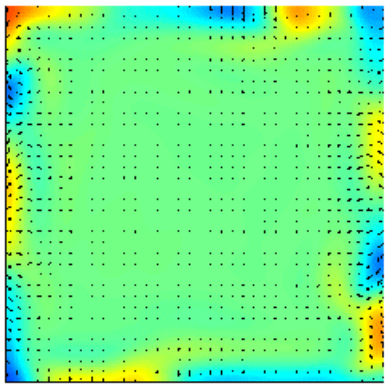

Fig. 5. Temperature field (background) and velocity components (vectors in foreground) in a horizontal plane in the middle of the box (Rot0 case).

(see Fig. 6). The number of plumes remains constant during this circulation. The circulation is also responsible for the shape of the plumes shown in Fig. 7.

We obtained the effect of "sidewall plumes" also in the Rot45 case. They appeared only on the sidewalls $y = 0$ and $y = a_y$ (parallel to the vector of rotation). The number of these plumes were not constant and they did not circulate. The convective vertical motion occurred again throughout the whole domain but was weaker.

3.3. Rotation and Adiabatic Cooling/Heating

In this section we will describe the results of the cases with mechanical heating Dis0, Dis45 and Dis90, where both rotation and adiabatic cooling/heating are present.

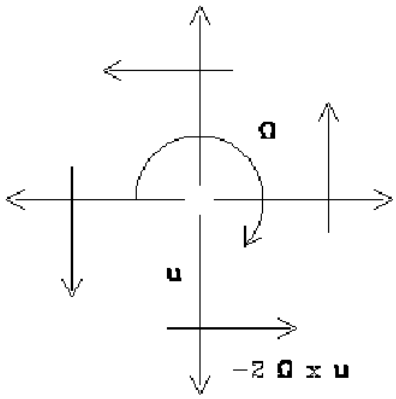

Fig. 6. Effect of the Coriolis force on motion perpendicular to the rotational axis.

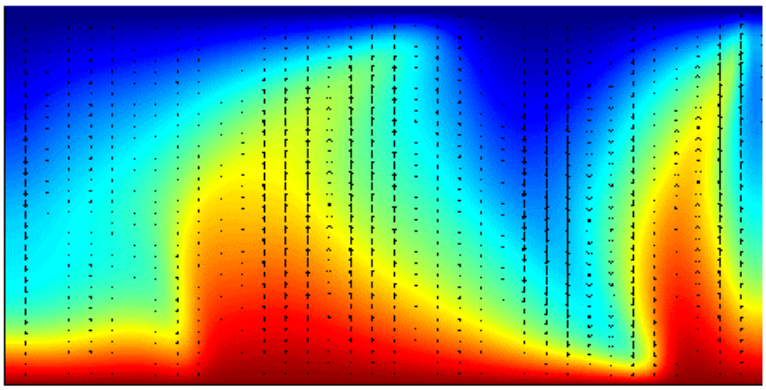

Fig. 7. Shape of circulating sidewall plumes in the (x, z) plane at $y = a_y$ (Rot0 case).

In Fig. 8 (Dis90 case) we display the contour plot of the temperature field and vector plot of the velocity field in the middle of the box in the vertical plane perpendicular to the rotational axis. The temperature field is characterized by small perturbations over the conductive profile. Although the temperature field is nearly static, the vector plot of velocities shows the circulation of the fluid. The direction of the most dominant circulation in the central area is opposite to the prescribed rotation in accord with the effect of the Coriolis force. Both the temperature field and the velocity field are nearly independent of the x-direction because the conditions are satisfied by the validity of the Taylor-Proudman theorem.

To show the differences between the Dis90 and Rot90 cases, we present the contour plots of the perturbation of temperature over the conductive profile for both cases (Fig. 9). While the maximum of these perturbations is ≈ 0.6 in the Rot90 case, including adiabatic heating and viscous dissipation (case Dis90) decreases the maximum to ≈ 0.05. We quantify the influences of both adiabatic heating and shear dissipation by the global quantities Λ and Φ, respectively:

$$\Lambda = \frac{1}{a_x a_y} \int_0^{a_x} \int_0^{a_y} \int_0^1 \left| Dn\left(T + T_\Delta\right) u_x \right| dx\, dy\, dz \,, \tag{40}$$

$$\Phi = \frac{1}{a_x a_y} \int_0^{a_x} \int_0^{a_y} \int_0^1 \left[PrDn\left(Ra\right)^{-1} \left(\sigma : \nabla \boldsymbol{u}\right) \right] dx\, dy\, dz \,. \tag{41}$$

The integrands consist of the adiabatic and/or dissipative term of energy equation (16). The time histories of these quantities over a couple of turnovers are shown in Fig. 10. The value of Φ is about three orders of magnitude less than the value of Λ. Thus the effect of dissipation is negligible and adiabatic heating is the only physical mechanism responsible for the stabilizing of both the temperature and the velocity fields.

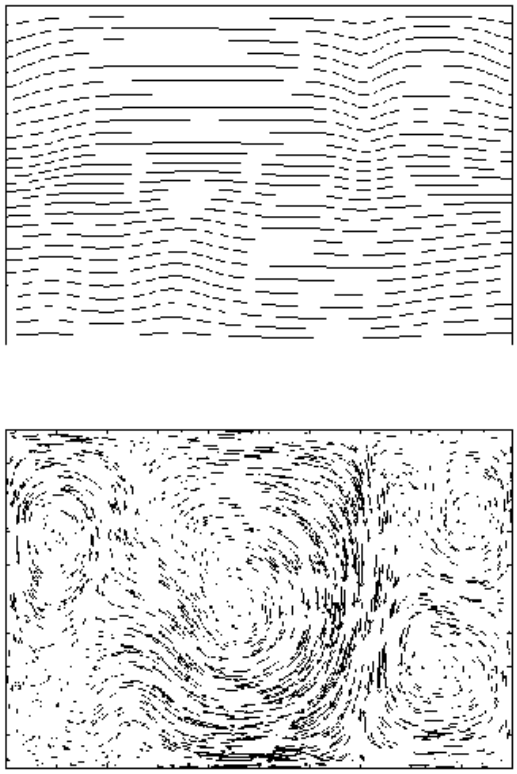

Fig. 8. Contour plot of temperature field (top) and vector plot of the velocity field (bottom) in the (y, z) plane at $x = a_x/2$ (Dis90 case).

In the Dis0 and Dis45 cases the kinetic energy and the heat flow passing through the bottom and top boundaries decrease more rapidly. The magnitude of dissipative heating was again negligible in comparison with the adiabatic cooling/heating.

4. CONCLUDING REMARKS

In this paper we have presented a new method of solving 3-D convection with rapid rotation by means of the vector potential/vorticity formulation combined with a higher-order finite-differencing scheme with irregularly spaced grid points. Velocity fields can be calculated from the vector potential with greater accuracy than the other approaches based on spheroidal and toroidal functions (e.g., *Kuang and Bloxham, 1999*). This ($\boldsymbol{A}$,$\boldsymbol{\omega}$) approach has been used with splines as a spatial discretized basis for 3-D thermal convection (*Malevsky, 1996*) and atmospheric dynamics (*Malevsky and Thomas, 1997*). What is novel here is the ability to incorporate variable-grid spacing while retaining the

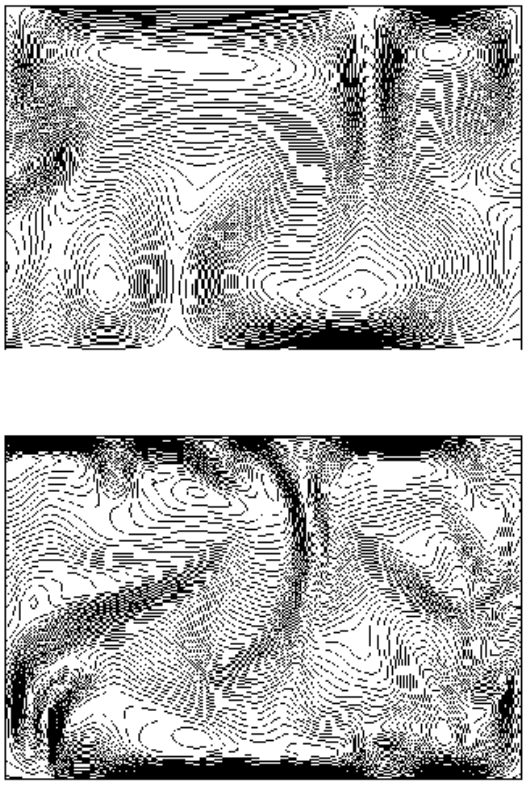

Fig. 9. Contour plots of the perturbations of temperature over the conductive profile for the Dis90 case (top) andRot90 case (bottom). Cross-section in the (y, z) plane $x = a_x/2$. Note the sharp gradients of temperature at the top and bottom boundary layers. We use different scaling as the maximum of the perturbations is approximately 0.05 (top) and 0.6 (bottom).

higher-order accuracy, a virtue which is the strength of the Fornberg scheme, now gaining more acceptance in the world of geophysical fluid dynamics (*Fornberg and Merrill, 1997; Larsen et al., 1997*). The ability of this spectral-like, finite-difference scheme to be applied to spherical geometry (*Fornberg, 1995; Fornberg and Merrill, 1997*) can greatly increase the computational efficiency of the geodynamo problem, which has been hampered by the use of spherical harmonics. These classical global basis functions impose a great computational burden on the calculation of the nonlinear terms which are needed for the high *Ra* regime involving high degree and order in the spherical harmonics, due to the costs in evaluating the nonlinear terms in the spatial domain.

We have obtained solutions which are characterized by thin top and bottom boundary layers and are well resolved by this variably spaced, higher-order scheme. Horizontal motions, screw motions and disconnection of the plumes due to the inertial forces

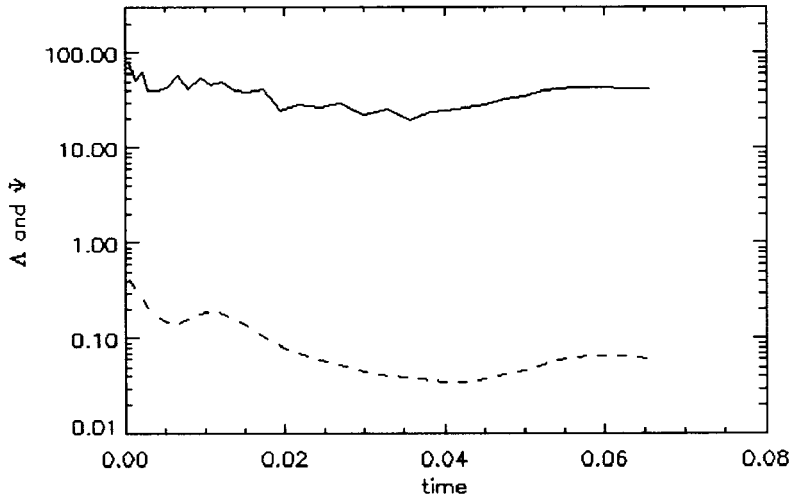

Fig. 10. Time evolution of Λ (adiabatic heating/cooling – solid line) and Φ (viscous heating – dashed line) for the Dis90 case.

represent the fundamental differences in comparison with the plume structures of mantle convection (*Moser et al., 1997* and *Larsen et al., 1997*).

Our numerical results also show that the adiabatic cooling/heating process can play an important role in thermal convection with rapid rotation. These results reinforce the findings of *Velímský and Matyska (2000)* in the magnetohydrodynamic problems, in which the thermal-mechanical influences of adiabatic heating/cooling have been included. The reason for this stabilizing effect is the much larger surface temperature at the core-mantle boundary than the temperature drop across the outer core. This can result in the adiabatic gradient which lies close to the conduction gradient. *Bercovici et al. (1992)* have already noted this effect in the high Prandtl number thermal convection. For thermal-chemical convection (*Hansen and Yuen, 1995*) the influence of a high surface temperature is even more pronounced than for pure thermal convection. This would imply that this adiabatic heating/cooling mechanism is even more relevant to the Earth's outer core, since planetary dynamos are probably driven in part by compositional buoyancy (*Lister and Buffet, 1995; Glatzmaier and Roberts, 1996*).

Acknowledgements: We thank Jakub Velímský, Ulli Hansen, Shuxia Zhang, Ladislav Hanyk, Andrei Malevsky and Bruce Buffet for fruitful discussions and encouragement in completing this work. We also acknowledge the constructive comments of an anonymous reviewer. This research has been supported by Research Project MŠMT J13/98: 113200004, the Charles University Grant 238/2001/B-GEO/MFF, the NATO Grant EST/CLG 977 093 and the Geosciences Program of the Dept. of Energy.

Manuscript received: 15 December 2000; Revisions accepted: 12 September 2001

References

Bercovici D., Schubert G. and Glatzmaier G.A., 1992. Three-dimensional convection of an infinite Prandtl number compressible fluid in a basally heated spherical shell. *J. Fluid Mech.*, **239**, 683–719.

Boehler R., 1996. Melting temperature of the Earth's mantle and core: Earth's thermal structure. *Annu. Rev. Earth Planet. Sci.*, **24**, 15–40.

Braginsky S.I. and Roberts P.H., 1995. Equations governing convection in the Earth's core and the geodynamo. *Geophys. Astrophys. Fluid Dynamics*, **79**, 1–97.

Breuer D. and Spohn T., 1993. Cooling of the Earth, Urey ratios, and the problem of potassium in the core. *Geophys. Res. Lett.*, **20**, 1655–1658.

Brummell N.H., Cattaneo F. and Toomre J., 1995. Turbulent dynamics in the solar convection zone. *Science*, **269**, 1370–1379.

Brummell N.H., Hurlburt N.E. and Toomre J., 1998. Turbulent compressible convection with rotation. II. Mean-flows and differential rotation. *Astrophys. J.*, **493**, 955–969.

Busse F.H., Grote E. and Tilgner A., 1998. On convection driven dynamos in rotating spherical shells. *Stud. geophys. geod.*, **42**, 211–223.

Cardin P. and Olson P., 1994. Chaotic thermal convection in a rapidly rotating spherical shell: consequences for flow in the outer core. *Phys. Earth Planet. Inter.*, **82**, 235–259.

Christensen U., 1989. Mantle rheology, constitution and convection. In: W.R. Peltier (Ed.), *Mantle Convection – Plate Tectonics and Global Dynamics*. Gordon and Breach Science Publishers, New York, 595–655.

Christensen U., Olson P. and Glatzmaier G.A., 1998. A dynamo model interpretation of geomagnetic field structures. *Geophys. Res. Lett.*, **25**, 1565–1568.

Christensen U. and Yuen D.A., 1985. Layered convection induced by phase transitions. *J. Geophys. Res.*, **90**, 10291–10300.

Demircan A., Scheel S. and Seehafer N., 2000. Heteroclinic behavior in rotating Rayleigh-Benard convection. *Europ. Phys. J. B*, **13**, 765–775.

Douglas J. Jr. and Rachford H.H., 1956. On the Numerical Solution of Heat Conduction Problems in Two and Three Space Variables. *Trans. Amer. Math. Soc.*, **82**, 421–430.

Fornberg B., 1992. Fast generation of weights in finite-difference formulas. In: G.D. Byrne and W.E. Schiesser (Eds.), *Recent Developments in Numerical Methods and Software for ODEs/DAEs/PDEs*. World Scientific Publ. Co., Singapore.

Fornberg B., 1995. A pseudospectral approach for polar and spherical geometries. *SIAM J. Sci. Comput.*, **16**, 1071–1081.

Fornberg B., 1996. *A Practical Guide to Pseudospectral Methods*. Cambridge Univ. Press, Cambridge.

Fornberg B. and Merrill D., 1997. Comparison of finite-difference and pseudospectral methods for convective flow over a sphere. *Geophys. Res. Lett.*, **24**, 3245–3248.

Glatzmaier G.A. and Roberts P.H., 1995. A three-dimensional convective dynamo solution with rotating and finitely conducting inner core and mantle. *Phys. Earth Planet. Inter.*, **91**, 63–75.

Glatzmaier G.A. and Roberts P.H., 1996. An inelastic evolutionary geodynamo simulation driven by compositional and thermal convection. *Physica D*, **97**, 81–94.

Hansen U.P. and Yuen D.A., 1995. Different consequences from compressibility on thermal and thermal-chemical convection in the Earth's outer core. *EOS*, **76**, 280–281.

Jarvis G.T. and McKenzie D.P., 1980. Convection in a compressible fluid with infinite Prandtl number. *J. Fluid Mech.*, **96**, 515–583.

Jarvis G.T. and Peltier W.R., 1989. Convection models and geophysical observations. In: W.R. Peltier (Ed.), *Mantle Convection – Plate Tectonics and Global Dynamics*, Gordon and Breach Science Publishers, New York, 479–593.

Kuang W. and Bloxham J., 1997. An Earth-like numerical dynamo model. *Nature*, **389**, 371–374.

Kuang W. and Bloxham J., 1999. Numerical modeling of magnetohydrodynamic convection in a rapidly rotating spherical shell: weak and strong field dynamo action. *J. Comput. Phys.*, **153**, 51–81.

Larsen T.B., Yuen D.A., Moser J. and Fornberg B., 1997. A high-order finite-difference method applied to large Rayleigh number mantle convection. *Geophys. Astrophys. Fluid Dynamics*, **84**, 53–83.

Lister J.R. and Buffet B.A., 1995. The strength and efficiency of thermal and compositional convection in the geodynamo. *Phys. Earth Planet. Inter.*, **91**, 17–30.

Malevsky A.V., 1996. Spline-characteristic method for simulation of convective turbulence. *J. Comput. Phys.*, **123**, 466–475.

Malevsky A.V. and Thomas S.J., 1997. Parallel algorithms for semi-Lagrangian advection. *J. Numer. Methods Fluids*, **25**, 455–473.

Merilees P.E., 1973. The pseudospectral approximation applied to the shallow water equations on a sphere. *Atmosphere*, **11**, 13–20.

Merilees P.E., 1974. Numerical experiments with the pseudospectral method in spherical coordinates. *Atmosphere*, **12**, 77–96.

Moser J., 1994. *Mantle Dynamics and Rotation of the Earth*. Ph.D. Thesis, Faculty of Mathematics and Physics, Charles University, Prague.

Pedlosky J., 1987. *Geophysical Fluid Dynamics*, Springer-Verlag, pp. 43–50.

Roberts P.H., 1992. Dynamo theory. In: D.A. Yuen (Ed.), *Chaotic Processes in the Geological Sciences, The IMA Volumes in Mathematics and its Applications*, **Vol. 41**, Springer-Verlag, New York, pp. 237–280.

St. Pierre M.G., 1996. On the local nature of turbulence in Earth's outer core. *Geophys. Astrophys. Fluid Dynamics*, **83**, 293–306.

Sun Z.P. and Schubert G., 1995. Numerical simulations of thermal convection in a rotating spherical fluid at high Taylor and Rayleigh numbers. *Phys. Fluids*, **7**, 2686–2699.

Tritton D.J., 1988. *Physical Fluid Dynamics*, 2nd edn., Oxford Univ. Press, New York.

Velímský J. and Matyska C., 2000. The influence of adiabatic heating/cooling on magnetohydrodynamic systems. *Phys. Earth Planet. Inter.*, **117**, 197–207.

Vitásek E., 1987. *Numerické Metody*, SNTL, Praha, 136–139 (in Czech).